Importance of bulk excitations and coherent electron-photon-phonon scattering in photoemission from PbTe(111): *Ab initio* theory with experimental comparisons

J. Kevin Nangoi, Siddharth Karkare, Ravishankar Sundararaman, Howard A. Padmore, and Tomás A. Arias

Phys. Rev. B **104**, 115132 — Published 17 September 2021

DOI: 10.1103/PhysRevB.104.115132

The importance of bulk excitations and coherent electron-photon-phonon scattering in photoemission from PbTe(111): *Ab initio* theory with experimental comparisons

J. Kevin Nangoi,[1,*] Siddharth Karkare,[2] Ravishankar Sundararaman,[3] Howard A. Padmore,[4] and Tomás A. Arias[1]

[1] *Department of Physics, Cornell University, Ithaca, New York 14853, USA*
[2] *Department of Physics, Arizona State University, Tempe, Arizona 85287, USA*
[3] *Department of Materials Science and Engineering, Rensselaer Polytechnic Institute, Troy, New York 12180, USA*
[4] *Lawrence Berkeley National Laboratory, 1 Cyclotron Rd., Berkeley, California 94720, USA*

This manuscript presents, to our knowledge, the first fully *ab initio* many-body photoemission framework that includes coherent three-body electron-photon-phonon scattering to predict the transverse momentum distributions and the mean transverse energies (MTEs) of bulk photoelectrons from single-crystal photocathodes. The need to develop such a theory stems from the lack of studies that provide complete understanding of the underlying fundamental processes governing the transverse momentum distribution of photoelectrons emitted from single crystals. For example, initial predictions based on density-functional theory calculations of effective electron masses suggested that the (111) surface of PbTe would produce very small MTEs (≤ 15 meV), whereas our experiments yielded MTEs *ten to twenty* times larger than these predictions and also exhibited a lower photoemission threshold than predicted. The *ab initio* framework presented in this manuscript correctly reproduces both the magnitude of the MTEs from our measurements in PbTe(111) and the observed photoemission below the predicted threshold. Our results show that *both* photoexcitations into states that propagate in the bulk of the material *and* coherent many-body electron-photon-phonon scattering processes, which initial predictions ignored, play surprisingly important roles in photoemission from PbTe(111). Finally, from the lessons learned, we recommend a procedure for rapid computational screening of potential single-crystal photocathodes for applications in next-generation ultrafast electron diffraction and X-ray free-electron lasers, which will enable significant advances in condensed matter research.

I. INTRODUCTION

Mean transverse energy (MTE), the average kinetic energy of photoemitted electrons *parallel* to a photocathode surface, is a key quantity that limits the brightness of state-of-the-art laser-driven electron sources[1,2] used, for example, in ultrafast electron diffraction (UED)[3] and X-ray free-electron lasers (XFELs).[1,4] Reducing the MTE increases the electron beam brightness, which increases the spatial resolution of UED[5–9] and the maximum lasing photon energy of XFELs.[5,8,10,11] Increased electron beam brightness also will enable more thorough and accurate studies of various physical phenomena, including the ultrafast photo-induced metal-insulator transition of VO_2[12] and ultrafast photo-conversion dynamics in rhodopsin.[13]

In the absence of a comprehensive theory, early efforts to reduce the mean transverse energy involve operating photocathodes both at cryogenic temperatures and near the photoemission threshold.[14–16] However, these conditions result in very low quantum efficiency, the number of emitted photoelectrons per incident laser photon, and thus can lower the overall beam brightness despite the reduced MTE.[16] To address this limitation, more recent efforts to lower the MTE without sacrificing quantum efficiency focus on *single-crystal* photocathodes, which possess well-defined band structures that can be exploited to produce low-MTE electron beams.[16] Karkare *et al.*[8] presented one of the first successful experimental attempts to reduce the MTE using single-crystal photocathodes. They found that single-crystal Ag(111) reduces MTEs below that of polycrystalline Ag[17] and yields a significantly larger quantum efficiency than a typical polycrystalline metal due to the high density-of-states close to the Fermi level provided by a Shockley surface state.[8]

Despite the recent experimental progress with single-crystal photocathodes, there are to date no fully *ab initio* studies exploring the fundamental underlying physics and predicting the resulting MTE. Early photocathode MTE theory focused primarily on polycrystals or photocathodes with disordered surfaces and used semi-empirical approaches.[14,15,18–21] Schroeder and Adhikari[22] do consider single-crystal photocathodes, but calculate the MTE by considering only electrons that originate from bulk states near the Fermi level and treating them as free electrons. Karkare *et al.*[2] developed a theoretical model that explains their MTE measurements on Ag(111)[8] by using the nearly free-electron model, a good approximation for only a limited number of metals.[23] Adhikari *et al.*[5], Schroeder *et al.*[24], and Li and Schroeder[25] use the free-electron approximation informed with *ab initio* effective masses calculated from density-functional theory (DFT), but neglect the full band structure of the material. Finally, Li *et al.*[26] use the full DFT band structure, but approximate the photoexcitation transition rates as uniform instead of calculating them *ab initio* from the appropriate transition matrix elements.

* Corresponding author. Email: jn459@cornell.edu

Beyond not being fully *ab initio*, most of the above single-crystal MTE studies assume direct photoexcitation into states that propagate only in vacuum. In reality, electrons also transition into states that both propagate in vacuum and extend throughout the bulk of the material. Such transitions can become the dominant process because, at typical operating laser energies, laser photons penetrate many atomic layers beneath the surface and can excite large numbers of electrons within the bulk region. For example, in PbTe, at the laser energies of interest (∼4–5 eV), photons have a characteristic absorption depth of ∼200 Å,[27] approximately thirty times the lattice constant.[28]

More recently, Camino *et al.*[29] did present a fully *ab initio* treatment of such bulk excitation processes in single crystals, but, due to a different focus, considered only quantum efficiency rather than the momentum and energy distributions of the emitted photoelectrons. They do consider a full, *ab initio* band structure and electronic transitions into states that propagate both in the material and in vacuum, with the transition rates calculated appropriately from first principles using Fermi's golden rule. However, due to their focus on quantum efficiency as opposed to MTE, Camino *et al.*[29] do not consider many-body excitation processes such as electron-phonon scattering, which can significantly alter the momentum distribution of excited electrons.[21]

Finally, a very recent work by Antoniuk *et al.*[30] considered bulk processes as well as intrinsic emittance ($\propto \sqrt{\text{MTE}}$, Ref. 9) in PbTe(111) and other materials. This work also neglected many-body processes such as electron-phonon scattering. Although Antoniuk *et al.* found good agreement between their calculations and the experimentally observed emittances from PbTe(111), to obtain such agreement they found it necessary to artificially scale the energies of the entire conduction band structure of PbTe by a constant multiplicative factor of ∼0.6.

Further progress in understanding the fundamentals of photoelectron distributions and MTEs thus requires *both* development of a new *ab initio* framework that considers many-body processes such as electron-phonon scattering *and* comparison with experiments exploring the full distributions of emitted photoelectrons. This manuscript presents just such a theory applicable to any single-crystal photocathode material, as well as comparisons to detailed experiments which measure not only the MTE but also the full distribution of transverse electron momenta. Furthermore, as Sec. III explains, the theory presented here includes a treatment of phonon effects on photoemission that goes beyond state-of-the-art photoemission theories.[31–34] As a case study, we consider single-crystal, semiconducting PbTe(111), finding good agreement with experiment, and we explain the significant discrepancies between our experimental measurements and previous theoretical estimates.[24,25] We find that consideration of electronic transitions into states that propagate both in the material and in vacuum and inclusion of coherent three-body electron-photon-phonon scattering to be key in explaining the observed MTEs, and that such consideration develops significant insight into the underlying physical mechanisms.

II. PREVIOUS THEORIES VS. EXPERIMENT

Motivated by the need for mean transverse energies below 10 meV for next-generation ultra-high-brightness applications,[35] previous density-functional theory studies[24,25] identified single-crystal, semiconducting PbTe(111) as capable of producing very low MTEs ($\leq$ 15 meV). These studies attribute the low MTEs to the small transverse effective masses associated with the valence band maximum of the material, as well as the impact of these small masses on direct transitions into states that propagate only in vacuum. Figure 1 illustrates such transitions for a photon energy of 4.4 eV, ∼0.2 eV above the calculated threshold from Refs. 24 and 25. Due to the small transverse effective masses, there are very few allowed transitions with small, non-zero transverse momenta along the W–L, L–K, X–L, and L–U directions. In contrast, there are a large number of transitions along Γ–L due to the larger effective mass along this direction. Because the Γ–L direction is parallel to the (111) surface normal, the corresponding photoelectrons will have essentially zero transverse momenta. These observations are what ultimately lead Refs. 24 and 25 to predict a very low MTE of $\leq$ 15 meV at this photon energy.

To explore the above predictions, we here measure the MTEs of photoelectrons emitted from an atomically ordered Pb-terminated PbTe(111) surface. We first prepared the surface by performing several cycles of ion-bombardment with 500 eV Ar^+ ions followed by annealing to 260°C on a commercially-purchased single-crystal PbTe(111) substrate.[36,37] We continued these cycles until the surface exhibited a sharp 1×1 hexagonal low-energy electron diffraction pattern and until Auger electron spectroscopy showed no surface contaminants. The light source generating the photoelectrons is a laser-based plasma lamp with a tunable wavelength monochromator[38] and a spectral width of 2 nm FWHM. The incident light is 35° off-normal and has a focused spot diameter of ∼150 μm on the PbTe(111) surface. We then accelerate the resulting photoelectron beam longitudinally to several kilovolts through a flat fine-mesh anode, allowing the beam to drift and expand from the effective point-spot on the PbTe(111) cathode under the transverse momenta of the photoelectrons. We obtain the transverse momentum distribution and MTE by measuring the size of the photoelectron beam after the acceleration with the setup given in Ref. 39.

Figure 2 contrasts the MTE predictions from Refs. 24 and 25 with our experimentally-measured MTEs at room temperature. Our measured values are up to twenty times larger than predicted. Moreover, unlike the predictions, our measurements exhibit non-monotonic behavior

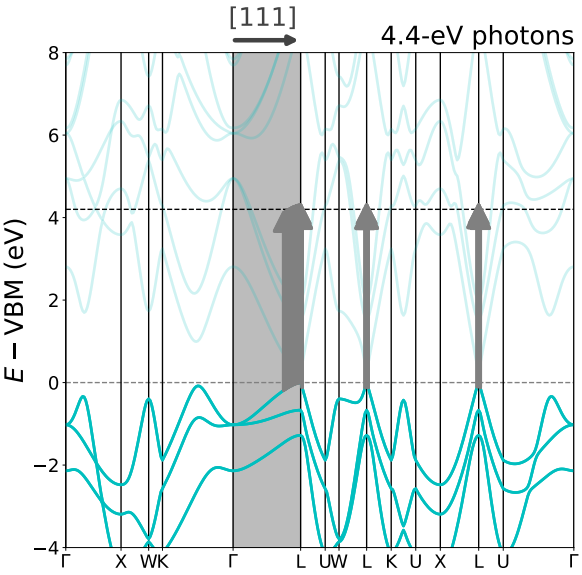

FIG. 1. Bulk band structure of PbTe: valence bands (solid curves), conduction bands (faint solid curves), high-symmetry path Γ–L parallel to the [111] surface normal direction (shaded region), valence band maximum (horizontal dashed line at 0), vacuum level from Refs. 24 and 25 (horizontal dashed line at 4.2 eV), and vertical transitions *directly into states that propagate only in vacuum* considered in Refs. 24 and 25 at a photon energy of 4.4 eV (vertical arrows). Arrow thickness corresponds to the number of available transitions and is proportional to both the density-of-states and the effective mass.

as a function of photon energy, as well as photoemission below the predicted threshold of 4.2 eV.

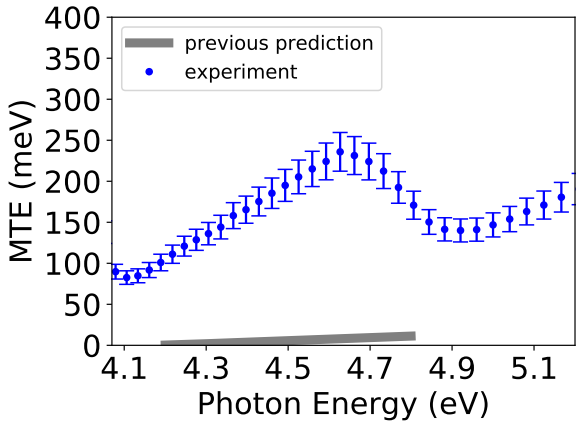

FIG. 2. Mean transverse energy (MTE) of photoelectrons emitted from PbTe(111) as a function of laser photon energy: our experimental results at room temperature (points with error bars) and previous predictions[24,25] (thick curve), which are 10–20× smaller than the observed MTEs and exhibit a higher threshold energy of 4.2 eV.

The significant discrepancies in magnitude and trend between our experimental MTEs and the predicted MTEs suggest additional processes to be at work. For example, excitations into states that not only propagate in vacuum but also extend deep into the bulk of the material may impact significantly the allowed transitions and affect the final distribution of emitted photoelectrons. Moreover, the observed photoemission below the predicted threshold suggests the presence of indirect photoexcitations, much like how indirect excitations in semiconductors can occur below the direct band gap. Therefore, coherent three-body electron-photon-phonon scattering also may play an important role in photoemission from PbTe(111). To explore these possibilities we now develop an *ab initio* framework capable of including these processes and predicting the momentum and energy distributions of the resulting photoelectrons.

III. FULLY *AB INITIO* APPROACH

To better explain our experimental observations of the MTE of PbTe(111), new theory must be developed. As observed in the previous section, such a theory not only must account for direct photoexcitations into states that propagate both in the material and in vacuum, but also must account for coherent electron-photon-phonon scattering. We previously reported in conference proceedings the results of calculations accounting for the above effects.[40] However, those calculations did not account for a number of other important factors. First, the finite linewidths of the intermediate electron states during the electron-photon-phonon scattering process can impact significantly the indirect photoexcitation transition rates and thus must be included in the calculations. Second, an excited Bloch state in the material couples to *not merely* a single outgoing plane-wave component in the vacuum, *but to all* plane-wave components whose momenta along the surface differ by reciprocal lattice vectors of the two-dimensional surface lattice. Third, the laser light in the experiment may not be of a single polarization, but may be unpolarized, as in our experiments. Finally, as is well known, band gaps calculated using semi-local density-functional theory can be inaccurate and often can be corrected through the standard so-called "scissors operator",[41,42] a procedure we had not yet applied.

The following subsections lay out our final method for calculating photoemission, transverse momentum distributions, and MTEs. First, Subsection III A describes the overall framework which we use to address all of the above issues and to calculate the transverse momentum distributions and MTEs. Subsections III B, III C, and III D then give details, respectively, of how we compute the photoexcitation transition rates, of how we calculate the probabilities of transmission into vacuum, and of the specific computational aspects of the underlying calculations.

A. Overall Framework

This subsection describes our general photoemission framework, which is applicable to single-crystal metallic as well as semiconducting photocathodes and is equivalent to the one-step photoemission model[2,31–34,43–50] in the limit "where the photoelectron escape depths are long,"[44] corresponding to our present work which focuses on bulk processes. Furthermore, our framework goes beyond existing *ab initio* one-step photoemission theories because we also include coherent electron-photon-phonon scattering explicitly, instead of implicitly through the optical potential method as in Refs. 31, 32, and 50, or through Debye-Waller-like theory as in Refs. 33 and 34. These other works make predictions that agree well with net photocurrent experiments and with band structures obtained from angle-resolved photoemission spectroscopy. However, the focus of our work here is specifically on the transverse momentum distributions of photoemitted electrons. More accurate determination of these distributions requires explicit consideration of the momenta and matrix elements of the phonons that scatter the electrons, and thus requires the more detailed accounting of phonon effects that our method provides.

As described in previous sections, the present work considers photoelectrons that originate from states that propagate in and are bound to the photocathode material and then transition into higher-energy states that propagate both in the material and in vacuum. Far from the surface of the material and deep into the bulk, both these higher-energy states and the bound states can be represented accurately as linear combinations of pure bulk Bloch states. Because of this, the bulk Bloch basis is an equivalent choice of basis for calculation of processes occurring in the bulk of the material. Given our focus on bulk photoexcitations, we thus choose the bulk Bloch basis as the most computationally convenient for all of our calculations.

Figure 3 illustrates the photoemission processes that we consider. First, a photon excites an electron from an occupied bulk Bloch state at band b into a higher-energy bulk Bloch state at band b' through either direct photoexcitation (1a), or phonon-mediated photoexcitation (1b), during which the electron absorbs the photon while either coherently absorbing or emitting a phonon. The higher-energy bulk Bloch state involved in the transition is a component of a coherent outgoing scattering state, which, deep into the material or far out into the vacuum, respectively, can be described as either a superposition of pure Bloch waves or a superposition of plane waves. As Fig. 3(2) illustrates, on the material side of the interface, the state will appear as a combination of the *excited* Bloch state at bulk band b' (which will have a group velocity toward the surface if the electron is ultimately to be emitted) and a set of *reflected* Bloch waves due to interaction with the surface. Similarly, far into the vacuum, the excited state will appear as a superposition of outgoing *transmitted* plane waves. The phases of all of the above superposed components must align at all points that are equivalent by the two-dimensional translational symmetry of the surface, and thus the crystal momentum component parallel to the surface must be conserved.[20] Specifically, for each plane-wave component $|\mathbf{q}\rangle$ of the outgoing wave in the far field of the vacuum, the parallel component of the wave vector $\mathbf{q}$ must match the sum of the parallel component of the excited Bloch state's crystal momentum $\mathbf{k}_f$ and a reciprocal lattice vector $\mathbf{G}_s$ of the two-dimensional surface: $\mathbf{q}_\parallel = \mathbf{k}_{f\parallel} + \mathbf{G}_s$. As Appendix A shows, for any three-dimensional bulk lattice and any surface, the surface reciprocal lattice vectors $\mathbf{G}_s$ correspond precisely to the projections $\mathbf{G}_\parallel$ onto the surface plane of all of the reciprocal lattice vectors $\mathbf{G}$ of the bulk crystal, allowing us to write

$$\mathbf{q}_\parallel = \mathbf{k}_{f\parallel} + \mathbf{G}_\parallel. \tag{1}$$

In addition to the parallel component of the momentum, the total energy also must be conserved during surface transmission,[20] so that the total kinetic energy $T(\mathbf{q})$ of the outgoing plane-wave component $|\mathbf{q}\rangle$ is

$$T(\mathbf{q}) = E_{\mathbf{k}_f,b'} - W, \tag{2}$$

where $E_{\mathbf{k}_f,b'}$ is the energy of the excited bulk Bloch state $|\mathbf{k}_f, b'\rangle$ relative to the same reference with which the work function W is determined. Equations (1) and (2) then yield the perpendicular component of the wave vector $\mathbf{q}$,

$$q_\perp(\mathbf{k}_f, b', \mathbf{G}_\parallel) \equiv \frac{\sqrt{2m_e T_\perp^{\mathbf{k}_f,b',\mathbf{G}_\parallel}}}{\hbar}, \tag{3}$$

where the kinetic energy in the direction perpendicular to the surface is

$$T_\perp^{\mathbf{k}_f,b',\mathbf{G}_\parallel} = E_{\mathbf{k}_f,b'} - W - \frac{\hbar^2}{2m_e}|\mathbf{k}_{f\parallel} + \mathbf{G}_\parallel|^2. \tag{4}$$

With the above ingredients in place, the mean-transverse energy is then the weighted average of the transverse kinetic energy of the plane-wave component $|\mathbf{q}(\mathbf{k}_f, b', \mathbf{G}_\parallel)\rangle$ over all values of $\mathbf{k}_f$, b', and $\mathbf{G}_\parallel$,

$$\mathrm{MTE}(\Omega) = \frac{\sum_{\mathbf{k}_f,b',\mathbf{G}_\parallel} \nu(\Omega, \mathbf{k}_f, b')\; t(\mathbf{k}_f, b', \mathbf{G}_\parallel)\; T_\parallel(\mathbf{k}_{f\parallel}, \mathbf{G}_\parallel)}{\sum_{\mathbf{k}_f,b',\mathbf{G}_\parallel} \nu(\Omega, \mathbf{k}_f, b')\; t(\mathbf{k}_f, b', \mathbf{G}_\parallel)}, \tag{5}$$

where the terms in the above expression are defined as follows. First, at photon energy $\hbar\Omega$ the photoexcitation transition rate $\nu(\Omega, \mathbf{k}_f, b')$ includes transitions from all possible initial bulk Bloch states to a particular excited bulk Bloch state $|\mathbf{k}_f, b'\rangle$ at momentum $\mathbf{k}_f$ and band b'. Second, $t(\mathbf{k}_f, b', \mathbf{G}_\parallel)$ is the transmission probability for the excited bulk Bloch state $|\mathbf{k}_f, b'\rangle$ to ultimately emerge as the plane-wave $|\mathbf{q}(\mathbf{k}_f, b', \mathbf{G}_\parallel)\rangle$ in vacuum. Third, $T_\parallel(\mathbf{k}_{f\parallel}, \mathbf{G}_\parallel) = (\hbar^2/2m_e)|\mathbf{k}_{f\parallel} + \mathbf{G}_\parallel|^2$ is the transverse kinetic energy of the plane-wave component $|\mathbf{q}(\mathbf{k}_f, b', \mathbf{G}_\parallel)\rangle$. The next subsections describe the calculation of $\nu(\Omega, \mathbf{k}_f, b')$ and $t(\mathbf{k}_f, b', \mathbf{G}_\parallel)$, respectively.

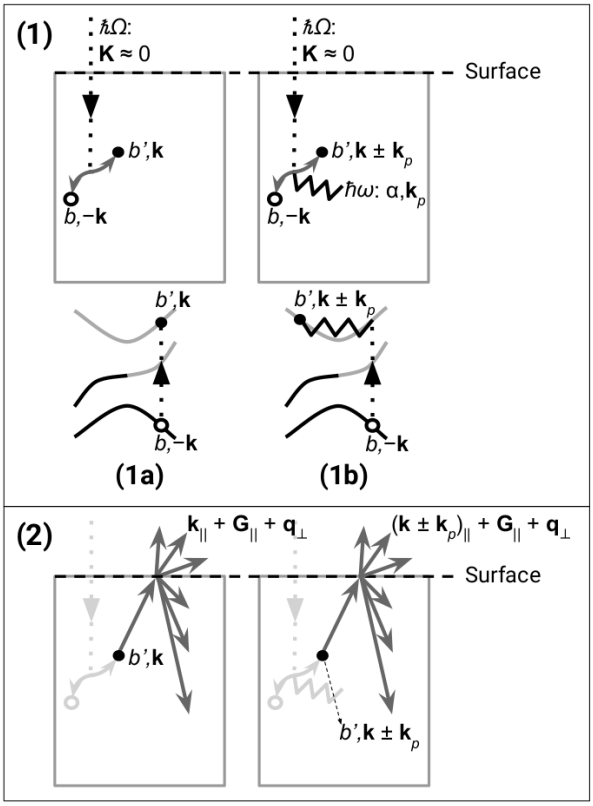

FIG. 3. Steps of the many-body coherent photoemission process, including direct photoexcitation (1a) and phonon-mediated photoexcitation (1b) into a bulk Bloch wave component of a state that propagates both in the material and in vacuum, and finally transmission of the said Bloch component into vacuum (2): incoming photon of momentum $\mathbf{K} \approx 0$ and energy $\hbar\Omega$ (dotted arrow), absorbed/emitted phonon of branch α, momentum $\mathbf{k}_p$, and energy $\hbar\omega$ (jagged line), resulting electron in Bloch band b' with momentum $\mathbf{k}$ or $\mathbf{k} \pm \mathbf{k}_p$ (filled circle), resulting hole in Bloch band b with momentum $-\mathbf{k}$ (open circle), and excited state with both material and vacuum components, consisting of a Bloch wave in the far field of the material traveling toward the surface (upward solid arrow pointing away from the filled circle), a superposition of reflected Bloch waves in the far field of the material (downward solid arrows), and a superposition of plane waves in the far field of the vacuum (upward solid arrows pointing away from the surface), each of which has a momentum $\mathbf{q} = \mathbf{k}_\parallel + \mathbf{G}_\parallel + \mathbf{q}_\perp$ or, if a phonon is involved, $\mathbf{q} = (\mathbf{k} \pm \mathbf{k}_p)_\parallel + \mathbf{G}_\parallel + \mathbf{q}_\perp$.

Finally, we note that, from Eq. (5), it is apparent that the transverse momentum distribution of the photoelectrons is the transverse momentum $\mathbf{k}_{f\parallel} + \mathbf{G}_\parallel$ weighted by the product $\nu(\Omega, \mathbf{k}_f, b')\ t(\mathbf{k}_f, b', \mathbf{G}_\parallel)$.

B. Photoexcitation Transition Rates

At a particular crystal momentum $\mathbf{k}$, a direct transition vertically excites an electron into a higher-energy band at the same $\mathbf{k}$, because at photon energies of interest (few eVs), the photon momenta are $\sim 10^3$ smaller than the typical electronic crystal momenta. A phonon-mediated transition, however, excites an electron into a higher-energy state at a different crystal momentum $\mathbf{k}' \neq \mathbf{k}$, because unlike photons, phonons can have arbitrary crystal momenta.

Within the dipole approximation,[51,52] first-order perturbation theory (Fermi's golden rule) and second-order perturbation theory give the following transition rates of the direct photoexcitations and the phonon-mediated photoexcitations,[53]

$$\nu^{\mathbf{k},b'\leftarrow b}_{\text{direct}} = \frac{2\pi}{\hbar}\frac{e^2}{m_e^2}(f_{\mathbf{k},b} - f_{\mathbf{k},b'})\delta(E_{\mathbf{k},b'} - E_{\mathbf{k},b} - \hbar\Omega) \times |(\mathbf{A}\cdot\mathbf{p})_{\mathbf{k},b'\leftarrow b}|^2 \quad (6)$$

$$\nu^{\mathbf{k}',b'\leftarrow\mathbf{k},b}_{\text{phonon}} = \frac{2\pi}{\hbar}\frac{e^2}{m_e^2}(f_{\mathbf{k},b} - f_{\mathbf{k}',b'})\sum_{\alpha\pm}\Bigg\{\left(n_{\mathbf{k}'-\mathbf{k},\alpha} + \frac{1}{2} \mp \frac{1}{2}\right) \times \delta(E_{\mathbf{k}',b'} - E_{\mathbf{k},b} - \hbar\Omega \mp \hbar\omega_{\mathbf{k}'-\mathbf{k},\alpha}) \times \Bigg|\sum_m \Bigg(\frac{g^{\mathbf{k}'-\mathbf{k},\alpha}_{\mathbf{k}',b'\leftarrow\mathbf{k},m}(\mathbf{A}\cdot\mathbf{p})_{\mathbf{k},m\leftarrow b}}{E_{\mathbf{k},m} - E_{\mathbf{k},b} - \hbar\Omega + i\eta_{\mathbf{k},m}} + \frac{(\mathbf{A}\cdot\mathbf{p})_{\mathbf{k}',b'\leftarrow m}\, g^{\mathbf{k}'-\mathbf{k},\alpha}_{\mathbf{k}',m\leftarrow\mathbf{k},b}}{E_{\mathbf{k}',m} - E_{\mathbf{k},b} \mp \hbar\omega_{\mathbf{k}'-\mathbf{k},\alpha} + i\eta_{\mathbf{k}',m}}\Bigg)\Bigg|^2\Bigg\}, \quad (7)$$

where the relevant quantities are defined as follows. The indices b, b', and α label the initial bulk band, excited bulk band, and phonon branch, respectively, and the constants e and m_e are the electron charge and vacuum electron mass. The quantities f, E, n, ω, and Ω respectively are the electron Fermi occupancy, electron band energy, phonon Bose occupancy, phonon frequency, and photon frequency, and the $\mp$ sign labels phonon absorption/emission respectively. The matrix element $(\mathbf{A}\cdot\mathbf{p})_{\mathbf{k},j\leftarrow i} \equiv \langle \mathbf{k}, j|\mathbf{A}\cdot\mathbf{p}|\mathbf{k}, i\rangle$ is the electron-photon interaction matrix element, and $g^{\mathbf{k}'-\mathbf{k},\alpha}_{\mathbf{k}',j\leftarrow\mathbf{k},i}$ is the electron-phonon interaction matrix element between an initial electronic state $|\mathbf{k}, i\rangle$, a phonon of momentum $\mathbf{k}' - \mathbf{k}$ and branch α, and a final electronic state $|\mathbf{k}', j\rangle$. Finally, $\eta_{\mathbf{k},m}$ is the electron linewidth of the intermediate state of the phonon-mediated photoexcitation at a particular momentum $\mathbf{k}$ and band m.

The electron linewidth $\eta_{\mathbf{k},m}$ considered in this work is the sum of the contributions to the imaginary part of the self-energy from electron-electron and electron-phonon scattering at the intermediate state $|\mathbf{k}, m\rangle$,

$$\eta_{\mathbf{k},m} = \text{Im}\,\Sigma^{\text{e–e}}_{\mathbf{k},m} + \text{Im}\,\Sigma^{\text{e–ph}}_{\mathbf{k},m}, \quad (8)$$

where Ref. 53 gives the expressions for $\text{Im}\,\Sigma^{\text{e–e}}_{\mathbf{k},m}$ and $\text{Im}\,\Sigma^{\text{e–ph}}_{\mathbf{k},m}$.

Choosing the Coulomb gauge ($\nabla\cdot\mathbf{A} = 0$)[54] to quantize

the vector potential $\mathbf{A}$ reduces Equations (6) and (7) to

$$\nu_{\text{direct}}^{\mathbf{k},b'\leftarrow b} = \frac{2\pi}{\hbar}\frac{e^2}{m_e^2}|A_0(\Omega)|^2(f_{\mathbf{k},b}-f_{\mathbf{k},b'})\delta(E_{\mathbf{k},b'}-E_{\mathbf{k},b}-\hbar\Omega) \times \left|\hat{\boldsymbol{\epsilon}}(\Omega)\cdot\mathbf{p}_{\mathbf{k},b'\leftarrow b}\right|^2 \tag{9}$$

and

$$\begin{aligned}\nu_{\text{phonon}}^{\mathbf{k}',b'\leftarrow\mathbf{k},b} = \frac{2\pi}{\hbar}\frac{e^2}{m_e^2}&|A_0(\Omega)|^2(f_{\mathbf{k},b}-f_{\mathbf{k}',b'}) \\ &\times\sum_{\alpha\pm}\left\{\left(n_{\mathbf{k}'-\mathbf{k},\alpha}+\frac{1}{2}\mp\frac{1}{2}\right)\right. \\ &\times\delta(E_{\mathbf{k}',b'}-E_{\mathbf{k},b}-\hbar\Omega\mp\hbar\omega_{\mathbf{k}'-\mathbf{k},\alpha}) \\ &\times\left|\hat{\boldsymbol{\epsilon}}(\Omega)\cdot\sum_m\left(\frac{g^{\mathbf{k}'-\mathbf{k},\alpha}_{\mathbf{k}',b'\leftarrow\mathbf{k},m}\;\mathbf{p}_{\mathbf{k},m\leftarrow b}}{E_{\mathbf{k},m}-E_{\mathbf{k},b}-\hbar\Omega+i\eta_{\mathbf{k},m}}\right.\right. \\ &\left.\left.\left.+\frac{\mathbf{p}_{\mathbf{k}',b'\leftarrow m}\;g^{\mathbf{k}'-\mathbf{k},\alpha}_{\mathbf{k}',m\leftarrow\mathbf{k},b}}{E_{\mathbf{k}',m}-E_{\mathbf{k},b}\mp\hbar\omega_{\mathbf{k}'-\mathbf{k},\alpha}+i\eta_{\mathbf{k}',m}}\right)\right|^2\right\},\end{aligned} \tag{10}$$

where $\mathbf{p}_{\mathbf{k},j\leftarrow i}\equiv\langle\mathbf{k},j|\mathbf{p}|\mathbf{k},i\rangle$ is the momentum operator matrix element and $\hat{\boldsymbol{\epsilon}}(\Omega)$ is the polarization unit vector of the photon with energy $\hbar\Omega$ inside the bulk of the material. Finally, $A_0(\Omega)$ is the amplitude of the vector potential $\mathbf{A}$ at photon energy $\hbar\Omega$, which does not contribute to the final distribution of photoelectrons because of the normalization factor in Eq. (5).

At a particular photon energy $\hbar\Omega$, depending on the polarization of the incident laser photons in vacuum, the photons inside the material can have multiple polarizations that sum incoherently. Therefore, in general, the total rate $\nu(\Omega,\mathbf{k}_f,b')$ of all transitions into an excited bulk Bloch state $|\mathbf{k}_f,b'\rangle$ involving photons with energy $\hbar\Omega$ is

$$\nu(\Omega,\mathbf{k}_f,b') = \sum_{\hat{\boldsymbol{\epsilon}}(\Omega)} a(\hat{\boldsymbol{\epsilon}}(\Omega))\left\{\nu_d(\Omega,\mathbf{k}_f,b';\boldsymbol{\epsilon}(\hat{\Omega})) + \nu_p(\Omega,\mathbf{k}_f,b';\boldsymbol{\epsilon}(\hat{\Omega}))\right\}, \tag{11}$$

where $a(\hat{\boldsymbol{\epsilon}}(\Omega))$ is the weight of the photons with an energy $\hbar\Omega$ and a particular polarization $\hat{\boldsymbol{\epsilon}}(\Omega)$ inside the material, $\nu_d(\Omega,\mathbf{k}_f,b';\hat{\boldsymbol{\epsilon}}(\Omega))\equiv\sum_b\nu_{\text{direct}}^{\mathbf{k}_f,b'\leftarrow b}$ is the direct transition rate Eq. (9) summed over all initial bands, and $\nu_p(\Omega,\mathbf{k}_f,b';\hat{\boldsymbol{\epsilon}}(\Omega))\equiv\sum_{\mathbf{k}b}\nu_{\text{phonon}}^{\mathbf{k}_f,b'\leftarrow\mathbf{k},b}$ is the phonon-mediated transition rate Eq. (10) summed over all initial states.

Our experiments on PbTe(111) use *unpolarized* laser light with an angle of incidence $\approx 35°$ and with an undetermined azimuthal direction with respect to the underlying crystalline axes. To deal with the latter uncertainty, we have considered both of the two distinct high-symmetry incoming laser beam directions along the surface, $\pm[1\bar{1}0]$ and $\pm[11\bar{2}]$, ultimately finding very similar results. For any given incoming beam direction there is a unique s-polarization direction and a p-polarization direction inside the material determined by the angle of refraction, which at the photon energies of interest ($\sim$4–5 eV) vary in our material between 40° and 70°. We find that for both of our considered incoming directions, the corresponding s-polarization and the three p-polarizations we have considered (corresponding to the refracted angles of 40°, 60°, and 70°) all yield quantitatively similar results for the MTE as a function of photon energy at the photon energies of interest. Accordingly, for this work, we choose to focus on a single, representative laser light in the material consisting of an equal, incoherent mixture of an s-polarization in the $\pm[1\bar{1}0]$ direction and a p-polarization corresponding to a refracted angle of 60°.

C. Surface Transmission Probability

Two conditions determine whether an electron in an excited bulk Bloch state transmits into vacuum. First, the electron's group velocity must be in the direction toward the surface. Second, to avoid total internal reflection, the electron must couple to the plane-wave components in the far field of the vacuum that have positive kinetic energies in the direction perpendicular to the surface. As discussed in Sec. III A, surface transmission conserves both the total energy and the momentum component parallel to the surface,[20] and thus it is possible for the kinetic energy perpendicular to the surface to become negative. With these considerations and including the appropriate kinematic factors, the transmission probability $t(\mathbf{k}_f,b',\mathbf{G}_\parallel)$ from the bulk Bloch state $|\mathbf{k}_f,b'\rangle$ to the vacuum plane-wave component $|\mathbf{q}(\mathbf{k}_f,b',\mathbf{G}_\parallel)\rangle$ is then

$$t(\mathbf{k}_f,b',\mathbf{G}_\parallel) = \Theta\left(\mathbf{v}_{\text{group}}^{\mathbf{k}_f,b'}\cdot\hat{\mathbf{n}}\right)\;\Theta\left(T_\perp^{\mathbf{k}_f,b',\mathbf{G}_\parallel}\right) \times|D_{\mathbf{k}_f,b',\mathbf{G}_\parallel}|^2\frac{\left[(2/m_e)\;T_\perp^{\mathbf{k}_f,b',\mathbf{G}_\parallel}\right]^{1/2}}{\mathbf{v}_{\text{group}}^{\mathbf{k}_f,b'}\cdot\hat{\mathbf{n}}}, \tag{12}$$

where $\mathbf{k}_f$ and b' respectively label the crystal momentum and the band of the excited bulk Bloch state, and $\mathbf{G}_\parallel$ is the surface projection of the vector $\mathbf{G}$ in the reciprocal bulk lattice. In the above equation, $\Theta(x)$ is the Heaviside step function, $D_{\mathbf{k}_f,b',\mathbf{G}_\parallel}$ is the amplitude of the plane-wave component $|\mathbf{q}(\mathbf{k}_f,b',\mathbf{G}_\parallel)\rangle$ in vacuum, $\mathbf{v}_{\text{group}}^{\mathbf{k}_f,b'}\equiv(1/\hbar)\nabla_{\mathbf{k}_f}E_{\mathbf{k}_f,b'}$ is the group velocity of the excited electron in the material, $\hat{\mathbf{n}}$ is the unit vector of the surface normal (which is parallel to [111] in this work), and $T_\perp^{\mathbf{k}_f,b',\mathbf{G}_\parallel}$ is given by Eq. (4). The fraction in the above equation gives the appropriate kinematic factors as the ratio of the perpendicular group velocity of the plane-wave component $|\mathbf{q}(\mathbf{k}_f,b',\mathbf{G}_\parallel)\rangle$ in vacuum to the perpendicular group velocity of the excited bulk Bloch state $|\mathbf{k}_f,b'\rangle$ in the material.

Previous *ab initio* one-step photoemission theories have employed either the Korringa–Kohn–Rostoker method[33,34,46] or $\mathbf{k}\cdot\mathbf{p}$ perturbation theory combined with the extended linear augmented-plane-wave method[31,32,47–50] to calculate exact excited scattering states and extract $D_{\mathbf{k}_f,b',\mathbf{G}_\parallel}$, the amplitude of the plane-wave component $|\mathbf{q}(\mathbf{k}_f,b',\mathbf{G}_\parallel)\rangle$ in the far field of the vacuum. Such theories require solving the three-dimensional Schrödinger's equation with a potential corresponding to a semi-infinite slab of material and a semi-infinite slab of vacuum, which would radically complicate our framework for including coherent electron-phonon-photon processes. Due to our focus on bulk processes, for simplicity here we have considered instead approximating $D_{\mathbf{k}_f,b',\mathbf{G}_\parallel}$ in three different ways,

$$|D_{\mathbf{k}_f,b',\mathbf{G}_\parallel}|^2 \approx \begin{cases} |\sum_{\mathbf{G}_\perp} C_{\mathbf{k}_f,b',\mathbf{G}_\parallel+\mathbf{G}_\perp}|^2 & \text{(13a)} \\ \max\{|C_{\mathbf{k}_f,b',\mathbf{G}_\parallel+\mathbf{G}_\perp}|^2\}_{\mathbf{G}_\perp} & \text{(13b)} \\ |D|^2, & \text{(13c)} \end{cases}$$

where D is a non-zero constant and $C_{\mathbf{k}_f,b',\mathbf{G}}$ is the amplitude of the plane-wave component of the excited bulk Bloch state associated with the reciprocal lattice vector $\mathbf{G}$, so that the bulk Bloch state $|\mathbf{k}_f,b'\rangle$ in *real space* is $\psi_{\mathbf{k}_f,b'}(\mathbf{r}) = \sum_{\mathbf{G}} C_{\mathbf{k}_f,b',\mathbf{G}} \exp[i(\mathbf{k}_f+\mathbf{G})\cdot\mathbf{r}]$. The motivations for these approximations are as follows. Equation (13a) assumes that the plane-wave component $|\mathbf{q}(\mathbf{k}_f,b',\mathbf{G}_\parallel)\rangle$ equals the superposition of the plane-wave components of the excited Bloch state $|\mathbf{k}_f,b'\rangle$ that have the same $\mathbf{G}_\parallel$. Equation (13b) assumes that for each $\mathbf{G}_\parallel$, only the plane-wave component of $|\mathbf{k}_f,b'\rangle$ with the largest probability determines $|\mathbf{q}(\mathbf{k}_f,b',\mathbf{G}_\parallel)\rangle$. Lastly, Equation (13c) is the simple constant-amplitude approximation.

For PbTe(111), the above three approximations give quantitatively similar results for the MTE as a function of photon energy at photon energies of interest (∼4–5 eV). Also, we note that Ref. 30 reports a similar observation where, for PbTe(111), the calculated emittances associated with bulk processes ($\propto \sqrt{\text{MTE}}$, Ref. 9) at the same photon energy range are *not* sensitive to the functional forms of transmission probability considered there. These two observations suggest that for bulk photoemission processes in PbTe(111), the inclusion of exact excited scattering states (such as time-reversed low-energy electron-diffraction states[2,31–34,43–50]) would not affect the transmission probabilities significantly. Given this and because our three approximations give very similar results, we choose in this work to use Eq. (13c), the simplest approximation of the three we have considered, so that from here forward we use

$$t(\mathbf{k}_f,b',\mathbf{G}_\parallel) \approx \Theta\left(\mathbf{v}_{\text{group}}^{\mathbf{k}_f,b'}\cdot\hat{\mathbf{n}}\right)\ \Theta\left(T_\perp^{\mathbf{k}_f,b',\mathbf{G}_\parallel}\right) \times |D|^2 \frac{\left[(2/m_e)\ T_\perp^{\mathbf{k}_f,b',\mathbf{G}_\parallel}\right]^{1/2}}{\mathbf{v}_{\text{group}}^{\mathbf{k}_f,b'}\cdot\hat{\mathbf{n}}}. \quad (14)$$

D. Computational Details

Calculation of MTE (Eq. (5)) involves evaluating high-dimensional sums over continuous set of crystal momenta $\{\mathbf{k}\}$ using the Monte Carlo method. Here, we employ the the Wannier interpolation method[55] to efficiently interpolate the required quantities, such as electron linewidths and matrix elements, for arbitrary values of $\mathbf{k}$. This interpolation method involves expressing such quantities in a maximally-localized Wannier basis formed by linear combinations of Bloch wavefunctions,[55,56] which requires calculation of the electronic structure of the material.

To calculate the electronic structure of PbTe, we employ the plane-wave density-functional theory (DFT) framework, with the GGA-PBE exchange correlation functional,[57] fully-relativistic norm-conserving pseudopotentials[58] from the SG15 library,[59] and spin-orbit coupling as implemented in the JDFTx software framework.[60] Similar to Refs. 30, 61, and 62, we have found that, *without* spin-orbit coupling, using both non-relativistic and scalar-relativistic pseudopotentials for PbTe with GGA-PBE yields a band gap that exceeds the experimental gap. Furthermore, as Refs. 61 and 62 show, to acquire a band gap that does *not* exceed the experimental gap, we must include spin-orbit coupling. We indeed find that including spin-orbit coupling with fully-relativistic pseudopotentials yields a gap that underestimates the experimental value and in alignment with values reported in other works.[61,62] Therefore, in this work we have chosen to include spin-orbit coupling using fully-relativistic pseudopotentials.

The calculations of the bulk electronic structure employ a face-centered-cubic (FCC) primitive cell of PbTe, a plane-wave cutoff of 20 Hartrees, a Brillouin zone sampling mesh of $6\times6\times6$, and an optimized PbTe lattice constant of 6.57 Å (within 2% from the experimental value[28]). To deal with DFT band-gap underestimation arising from employing the semi-local GGA-PBE functional, we scissor the conduction band energies to match the experimental gap of 0.3 eV.[63] Using linear combinations of the bulk Bloch bands at energies from 4.8 eV below to 12.7 eV above the valence band maximum, we generate a maximally-localized Wannier basis set using a supercell of $6\times6\times6$ FCC primitive cells. This Wannier basis set reproduces the bulk band structure at the energy range from 4.8 eV below to 5.7 eV above the valence band maximum, which is sufficient to include all photoexcitations with photon energies of interest (∼4–5 eV). The determination of these Wannier functions and their use below in determining linewidths, matrix elements and MTEs are all based on the implementation of JDFTx[60] described in Ref. 53.

Because this work considers phonon-mediated photoexcitations, we also calculate the force matrix for bulk phonons and the electron-phonon matrix elements of PbTe using a modified version of the frozen phonon method, as implemented in JDFTx,[60] which allows calculations of phonons at arbitrary wave-vectors. These

calculations use a supercell of $3 \times 3 \times 3$ FCC primitive cells and DFT parameters corresponding to those of the bulk electronic structure calculations described above.

The phonon-mediated excitations also require calculation of the electron linewidths (Eq. (8)) for all bulk electronic states. The methods of these calculations are detailed elsewhere.[53] For this work, the calculation of the electron-electron scattering contribution to the linewidth uses a frequency grid resolution of 0.001 eV and a cutoff of ∼130 eV for the dielectric matrices. The calculation of the electron-phonon scattering contribution uses a fine wave-vector grid of $168 \times 168 \times 168$.

The surface transmission probability of a photoexcited electron (Eq. (14)) depends on the work function of the material surface. Although it is possible to calculate the work function of PbTe(111) *ab initio*,[24,25] the effective work function in our experiments can be quite different due to effects such as the surface condition of our sample and the Schottky effect.[15,25] Because careful measurements of the effective work function of our sample are not available, we determine the effective work function by comparing our calculated MTEs with our experimental MTEs. As Appendix B shows, a work function of 4.05 eV (at the low end of the range 4.1–4.9 eV reported in the literature[24,25,64–66]) results in the best agreement between our calculated and experimental MTEs as functions of photon energy.

Finally, to determine the MTEs, this work uses $\sim 1.5 \times 10^8$ Monte Carlo samples of crystal momenta $\mathbf{k}$ to converge our results in the photon energy range of interest (∼4–5 eV). To enumerate the possible outgoing plane waves, we include the $\mathbf{G}_\parallel$ vectors for the nearest neighbors of $\mathbf{G}_\parallel = 0$, the origin of the surface-projected reciprocal lattice. This range of $\mathbf{G}_\parallel$ is sufficient to cover the transverse momenta measured in our experiments.

IV. RESULTS AND DISCUSSION

A. Mean Transverse Energies

Figure 4 shows our experimental measurements and our theoretical results for the mean transverse energy of photoelectrons emitted from PbTe(111) as a function of laser photon energy and compares them with the previous predictions from Refs. 24 and 25. Note that these latter predictions consider only direct photoexcitations into states that propagate only in vacuum, whereas, as we have described in previous sections, our calculations include both direct and phonon-mediated photoexcitations into states that propagate both in the material and in vacuum. We find that our results far better reproduce the magnitude and general trends of the measured MTEs both below and above the calculated direct threshold of 4.27 eV. Although we do not reproduce the experimentally observed dip centered at 4.9 eV, we do find a leveling off of the increase in the MTE at similar energies. Section IV B explores this discrepancy in more detail, showing that this feature is likely due to photoexcitations into states that propagate only in vacuum. Also, we find that including only the direct excitations reproduces relatively well the MTEs above the calculated threshold, even though the *indirect* excitations above threshold actually account for at least ∼45% of the total number of emitted photoelectrons. Both the need to consider phonon-mediated processes below the direct threshold *and* the prevalence of such processes above threshold underscore the importance of indirect transitions due to phonon effects in photoemission from PbTe(111).

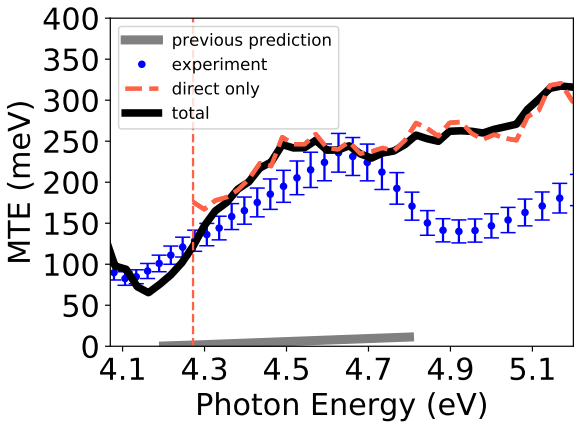

FIG. 4. Mean transverse energy (MTE) of photoelectrons emitted from PbTe(111) as a function of laser photon energy at room temperature: our experimental results (points with error bars), our calculations including direct and phonon-mediated excitations (solid curve), our calculations including solely direct excitations (dashed curve), previous predictions[24,25] (thick curve with small MTE values), and our calculated threshold of direct photoexcitation (vertical dashed line). Compared to previous predictions, which are an order of magnitude smaller, our calculations yield far better agreement with our experiments.

It is worth noting that Ref. 30 provides *ab initio* calculations of intrinsic emittances ($\propto \sqrt{\text{MTE}}$, Ref. 9) of photoelectrons emitted from PbTe(111) that, over the same photon energy range as in Fig. 4, seem to reproduce the measured MTEs we report here and in Ref. 40 *without* consideration of phonon-mediated photoexcitations or other indirect processes. However, as mentioned in Sec. I, to obtain such agreement, Ref. 30 artificially scales the energies of the entire density-functional theory (DFT) conduction band structure by a constant multiplicative factor of ∼0.6 to match the calculated effective mass at the conduction band minimum with the experimental value. Such a scaling significantly distorts the energy scales of the conduction states that actually participate in photoemission, which, due to the work function, are ∼4 eV or more above the conduction band minimum prior to scaling. For example, this scaling would reduce the photon energy corresponding to photoexcitations into the states at our calculated direct threshold from 4.27 eV down to an unreasonable value of ∼2.7 eV.

For PbTe, given that the DFT conduction band structure after a scissors operator and *without* scaling agrees quite well with established many-body GW calculations,[67] the agreement with experiments found in Ref. 30 appears to be fortuitous. On the other hand, here we find that we can improve the agreement with our experiments without the need for artificial scaling of the condition band energies by including indirect, phonon-mediated bulk photoexcitation processes.

The significance of phonon effects in photoemission from PbTe(111) suggests that operation at cryogenic temperatures might reduce the MTEs. To explore such effects, Fig. 5 contrasts our room-temperature results with what we predict for the MTEs at 30 K. Above the direct threshold of 4.27 eV, the MTEs at 30 K are approximately equal to the MTEs at room temperature as well as the MTEs due to direct processes only, which are not affected significantly by temperature. Below the direct threshold, we indeed predict a lowering of the MTEs when operating at 30 K. However, unlike in polycrystalline metallic photocathodes where the MTE is directly proportional to the thermal energy k_BT near and below threshold,[14] for single-crystal PbTe(111) we find a more complicated behavior and not nearly the expected factor of ten reduction. Simply lowering the operating temperature of single-crystal photocathodes is not guaranteed to provide a significant reduction in the MTE.

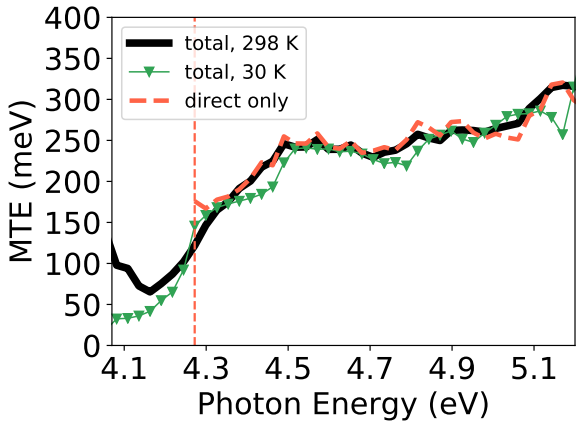

FIG. 5. Calculated MTE as a function of laser photon energy: with phonon effects at room temperature (solid curve), with phonon effects at 30 K (downward triangles), without phonon effects (dashed curve), and the threshold of direct photoexcitation (vertical dashed line).

Beyond not necessarily providing significant reduction in MTE, lowering the photocathode temperature reduces the number of phonons available for indirect photoexcitation processes and thus may lower the quantum efficiency, thereby actually reducing the overall beam brightness. Without lowering of the photocathode temperature as a guaranteed method, improving beam brightness from single-crystal photocathodes will require materials whose band structures allow photoexcitations of electrons with low transverse momenta even at room temperature. Discovery of such materials requires a deeper understanding of the transverse momentum distributions of emitted photoelectrons, which the next section explores.

B. Transverse Momentum Distributions

To further elucidate the photoemission process and to explore the origin of the lack of the dip near 4.9 eV in our predicted mean transverse energies (MTEs), we now explore the detailed transverse momentum distribution of the photoemitted electrons. This distribution is a two-dimensional histogram of the transverse momenta $\mathbf{k}_{f\parallel} + \mathbf{G}_\parallel$ of all emitted photoelectrons in the plane parallel to the surface. As discussed in Sec. III A, we can extract this histogram from our framework by taking the histogram weights to equal the product of the photoexcitation transition rate $\nu(\Omega, \mathbf{k}_f, b')$ (Eq. (11)) and the surface transmission probability $t(\mathbf{k}_f, b', \mathbf{G}_\parallel)$ (Eq. (14)). Figure 6 shows the room-temperature transverse momentum distributions at photon energies near and above the direct threshold of 4.27 eV, comparing the results from our calculations under various approximations with our experimental results.

The first two rows of Fig. 6 compare the results from considering the direct processes only with the results from including also the indirect processes. As indicated in the second row, although the indirect processes make a significant contribution, neither the indirect nor the direct processes completely dominate. Furthermore, we see that at the photon energies considered, above 4.3 eV the transverse momentum distributions from the direct-only processes are similar to the distributions from the combined direct and indirect processes, explaining why both the direct-only MTEs and the total MTEs are approximately equal above the direct threshold (Fig. 5). Finally, it is apparent from Fig. 6 that both the direct and phonon-mediated photoexcitations result in photoelectrons with primarily significant transverse momenta, thereby corresponding to the large calculated MTEs of a few hundred meV that we find above the direct threshold.

Figure 6 also compares our calculated distributions with our experimental results shown on the bottom-most row. Note that, unlike the calculated distributions on the second row, the experimental distributions *do not* show the three-fold symmetry of the (111) surface of PbTe, but show nearly cylindrical symmetry. We believe this is *not* due to polycrystallinity, because our sample shows a clear hexagonal pattern from low-energy electron diffraction experiments. We also believe that the smearing is *not* due to the detector resolution which is 0.01 Å^{-1}, significantly smaller than the characteristic size of the smearing which is on the order of 0.1 Å^{-1}. The cylindrical smearing is then likely due to other effects such as non-uniform electric fields on the photocathode surface. Possible causes of these fields include surface relaxations and reconstructions, as well as small rough patches and

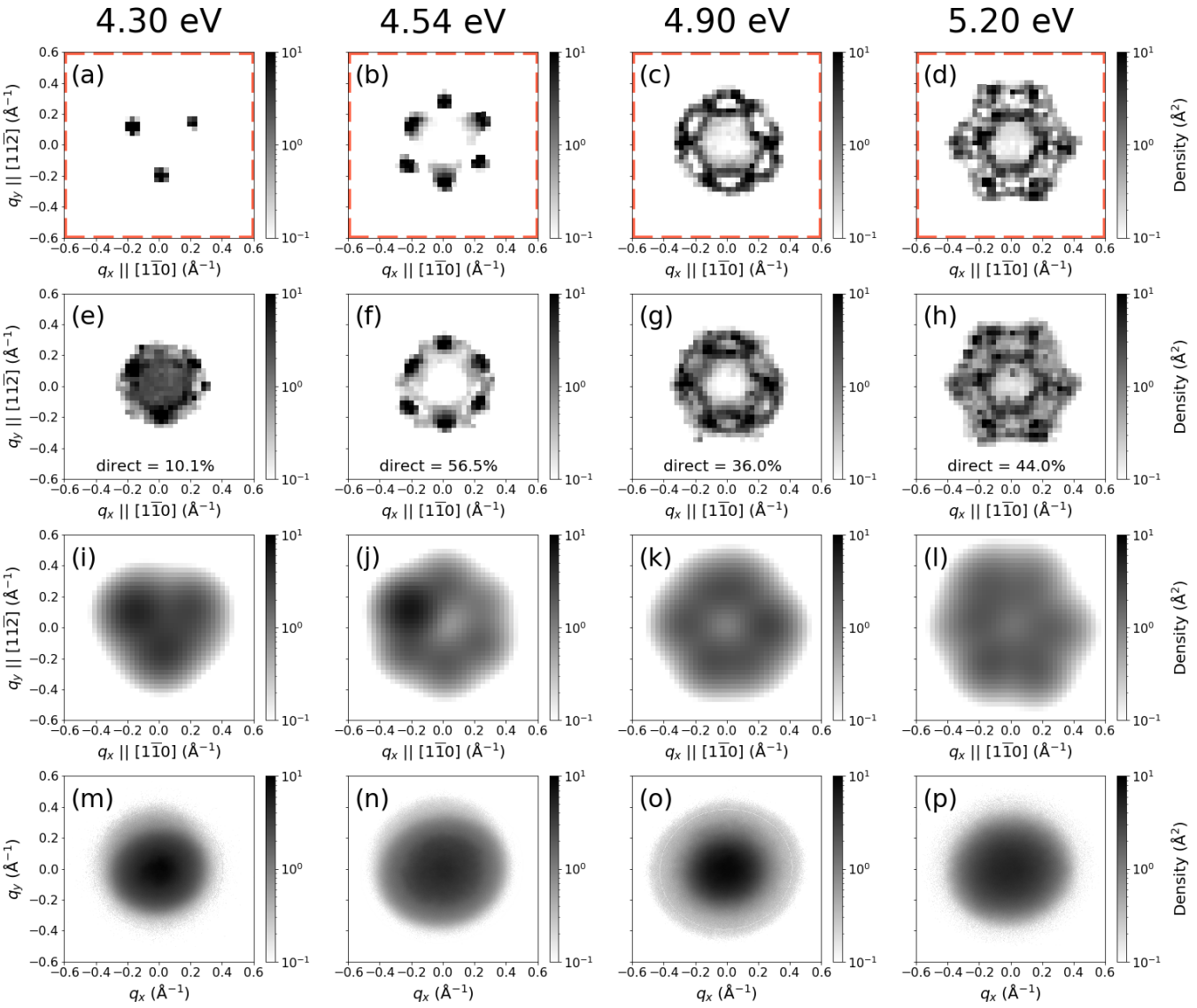

FIG. 6. Transverse momentum distributions, normalized as probability densities, on the $q_x q_y$ plane parallel to the (111) surface at four different photon energies near and above the direct threshold: distributions including only direct excitations (top row), distributions including both direct and phonon-mediated excitations (second row), fractions, in percents, of the probability densities that are due to direct excitations (second row, "direct"), distributions including both direct and phonon-mediated excitations with Gaussian smearing of RMS width 0.1 Å^{-1} (third row), and experimentally measured distributions (bottom row). The overall sizes and the trends of the distributions are consistent with the MTE data in Fig. 4.

atomic steps, all of which have been experimentally observed on PbTe(111).[36,68]

To account for the observed cylindrical smearing effects in a simplified way, the third row of Fig. 6 shows the results from the second row convolved with a two-dimensional Gaussian of RMS width 0.1 Å^{-1}, which gives the best overall agreement with the experimental distributions. The convolved distributions have similar sizes to the experimental distributions up until 5.2 eV, where the convolved distribution is noticeably larger than that observed experimentally, consistent with the larger predicted MTE in Fig. 4.

Contributing to our overprediction of MTEs at high photon energies is the fact that our convolved transverse momentum distributions remain somewhat "hollow" with low contributions in the center, as contrasted with our measured distributions which tend to be peaked at the center. One possible explanation for this difference is that our calculations exclude contributions from the photoelectrons that transition directly into states that propagate only in vacuum. As explained in Sec. II, among such electrons there are significant contributions from transitions along the Γ–L direction with zero transverse momenta, which would tend to fill in the distri-

butions and lower the predicted MTE. We believe that future work combining transitions into states that propagate both in the material and in vacuum with transitions into states that propagate only in vacuum will further improve the agreement between theory and experiment. In particular, we expect that doing this will reproduce the dip in MTE near 4.9 eV observed in Sec. IV A.

The above future work requires reformulating our photoemission theory in the geometry consisting of a material half-space and a vacuum half-space, which will allow us to include exact excited scattering states (such as time-reversed low-energy electron-diffraction states[2,31–34,43–50]). Such a formalism also will allow further improvements to our theory, including corrections due to surface effects such as surface relaxations, surface reconstructions, and rapid spatial variations of the electromagnetic field of laser light inside photocathode material.[69–73]

V. COMPUTATIONAL SEARCH FOR LOW-MTE SINGLE-CRYSTAL PHOTOCATHODES

The insights gained in the previous sections enable the development of an efficient computational screening procedure to search for single-crystal materials that yield photoelectrons with low mean transverse energies. Such screening must consider excitation into states that propagate both in the material and in vacuum as well as excitation into states that propagate only in vacuum, both of which must yield low MTEs. References 24 and 25 give an example of screening based on direct excitations into states that propagate only in vacuum. The remainder of this section focuses on important considerations when screening based on excitations into states that propagate both in the material and in vacuum.

For efficient screening, we suggest including at first only direct photoexcitations, not only because these excitations can contribute significantly to the MTEs, as in the case of PbTe(111) (Sec. IV B), but also because they are significantly less computationally demanding to evaluate. When considering only the direct processes, it may be tempting to use publicly-available band structures of prospective photocathode materials. Such band structures, however, generally explore only the high-symmetry paths in the Brillouin zone, which may result in failure to include important contributions from photoexcitation processes occurring at low-symmetry points. For example, Fig. 7(a) shows a bulk band structure that typically might be found for PbTe in public databases (for example, the Materials Project[74]) that show selected paths between the high-symmetry points in the face-centered-cubic Brillouin zone. We first eliminate the excited states that have *zero* surface transmission probabilities due to negative perpendicular kinetic energies or group velocities directed away from the surface. The remaining possible vertical transitions then indicate a direct threshold of 4.54 eV. In contrast, the actual threshold, which we find by considering all possible transitions in the Brillouin zone, is significantly lower, 4.27 eV (Sec. IV A).

To further illustrate the importance of considering all crystal momenta, Fig. 7(b) shows the transverse momentum distribution at a photon energy of 4.54 eV, superposed on the projection onto the surface plane of all high-symmetry paths available in the band structure in Fig. 7(a). The direct transitions along Γ–K shown in Fig. 7(a) correspond to the cluster of points about halfway along the projected Γ,L–K path in Fig. 7(b), which has two other copies due to symmetry as indicated in the figure. There are, however, three additional excitation pockets evident in Fig. 7(b) appearing at points that *do not* correspond to any points in Fig. 7(a), which shows no available transitions along any of the paths connecting Γ or L to X or U. This example demonstrates how *all* crystal momenta in the Brillouin zone must be considered to avoid false conclusions about the performance of single-crystal photocathode materials.

VI. CONCLUSIONS

This work describes, to our knowledge, the first fully *ab initio* many-body photoemission framework that includes coherent three-body electron-photon-phonon scattering for calculating the mean transverse energy (MTE) of single-crystal photocathodes. The framework uses the full bulk band structure of the material under study calculated using density-functional theory. Our framework also considers various physical processes relevant to photoemission, such as direct photoexcitation and phonon-mediated photoexcitation, whose transition rates we calculate from first principles. We use our *ab initio* framework to study the MTE and transverse momentum distribution from the (111) surface of PbTe as functions of laser photon energy. Our results explain the significant discrepancy between the magnitude of the previous MTE predictions[24,25] and the magnitude of our experimentally measured MTEs. Finally, the lessons learned from this case study of PbTe(111) allow us to recommend a computational screening procedure to find low-MTE single-crystal materials based on the photoelectrons that undergo direct photoexcitations.

Despite the good agreement between our calculated MTEs and our experimentally-measured MTEs from PbTe(111), several discrepancies remain. First, our calculated transverse momentum distributions show the three-fold symmetry of the PbTe(111) crystal surface, whereas our measured distributions show nearly cylindrical symmetry. We attribute this difference to some combination of surface reconstructions and relaxations, small rough patches, and atomic steps on the single-crystal surface of PbTe(111). Second, our calculated distributions tend to be hollow at the center, whereas our measured distributions tend to be peaked at the center. This difference is likely due to the contributions of the excited

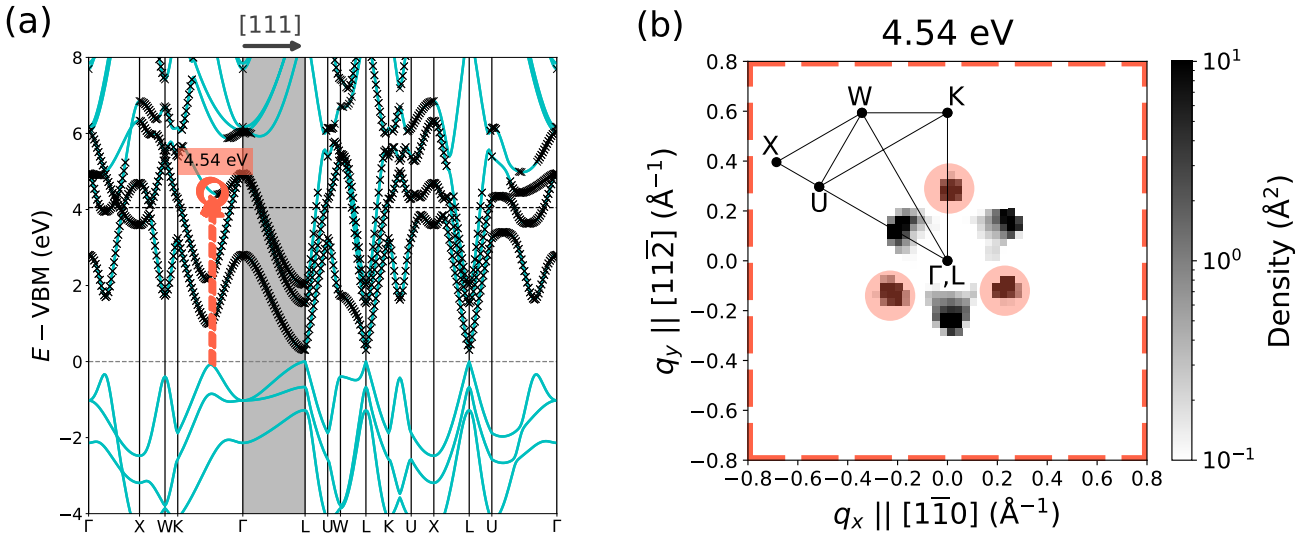

FIG. 7. (a) Bulk band structure of PbTe: bands (solid curves), high-symmetry path Γ–L parallel to the [111] surface normal direction (shaded region), valence band maximum (horizontal dashed line at 0), vacuum level (horizontal dashed line at 4.05 eV), conduction states with zero surface transmission probabilities (×), direct transitions occurring along high-symmetry paths at the apparent direct threshold of 4.54 eV (vertical dashed arrows), and conduction states corresponding to these direct transitions (circles). The arrow-circle pairs are located very close to each other, nearly halfway along Γ–K. (b) Transverse momentum distribution, normalized as probability density, including only direct processes at 4.54 eV (square pixels), projection onto the (111) surface plane of high-symmetry paths available in panel (a) (straight lines), and direct transitions depicted in panel (a) (square pixels highlighted by circles).

electrons that transition into states that propagate only in vacuum, which are not considered in this work and whose inclusion would likely improve our agreement with experiment.

We here also consider the effects of temperature, and find results suggesting that standard techniques such as lowering the photocathode temperature do not necessarily reduce the MTEs of single-crystal photocathodes. On the other hand, computational screening of single-crystal materials remains a viable pathway to produce photocathodes with low MTEs. In performing the screening, it is important to consider photoexcitations at *all* crystal momenta instead of only along high-symmetry paths in the Brillouin zone, and to consider transitions into states that propagate both in the material and in vacuum as well as transitions into states that propagate only in vacuum. Finally, once low-MTE candidates are identified, further computational studies using the approach we introduce here should be carried out to determine whether other processes, such as phonon-mediated photoexcitations, significantly affect the MTEs.

ACKNOWLEDGMENTS

This work was supported by the U.S. National Science Foundation under Award PHY-1549132, the Center for Bright Beams (J. K. N., T. A. A., S. K., H. A. P.), and by the Director, Office of Science, Office of Basic Energy Sciences of the U.S. Department of Energy, under Contracts No. KC0407-ALSJNT-I0013 and No. DE-AC02-05CH11231 (S. K., H. A. P.).

Appendix A: Proof that $\{\mathbf{G}_s\} = \{\mathbf{G}_\parallel\}$

Let $\mathcal{R}$ be a set containing all vectors $\mathbf{R}$ in a three-dimensional Bravais lattice and let $\mathcal{G}$ be the set containing all vectors $\mathbf{G}$ in the reciprocal lattice of $\mathcal{R}$. By definition,

$$\mathcal{R} \cdot \mathcal{G} \subset 2\pi\mathbb{Z}, \tag{A1}$$

where $\mathbb{Z}$ is the set of all integers and the dot product is defined as the set containing all possible dot products between the members of $\mathcal{R}$ and the members of $\mathcal{G}$.

For any $\mathcal{R}$ and any surface with unit normal vector $\hat{\mathbf{n}}$, *all* lattice vectors along the surface form a set $\mathcal{R}_s = \{\mathbf{R} \in \mathcal{R} : \mathbf{R} \cdot \hat{\mathbf{n}} = 0\} \subset \mathcal{R}$. The set $\mathcal{R}_s$ corresponds to a two-dimensional Bravais lattice because for any $\mathbf{R}_{s1}, \mathbf{R}_{s2} \in \mathcal{R}_s$, $\mathbf{R}_{s1} + \mathbf{R}_{s2} \equiv \mathbf{R}_3 \in \mathcal{R}$ and $\mathbf{R}_3 \cdot \hat{\mathbf{n}} = 0$, which imply that $\mathbf{R}_3 \in \mathcal{R}_s$.

Let $\mathcal{G}_\parallel$ be the set of all vectors in $\mathcal{G}$ projected onto the surface defined by the unit normal vector $\hat{\mathbf{n}}$: $\mathcal{G}_\parallel \equiv P\mathcal{G}$, where the projection operator $P = 1 - \hat{\mathbf{n}}\hat{\mathbf{n}}\cdot$ applied to the set $\mathcal{G}$ returns the set of the projections of all members of $\mathcal{G}$. The set $\mathcal{G}_\parallel$ forms a two-dimensional Bravais lattice because for any $\mathbf{G}_{\parallel 1}, \mathbf{G}_{\parallel 2} \in \mathcal{G}_\parallel$, there exist $\mathbf{G}_1, \mathbf{G}_2 \in \mathcal{G}$ such that $\mathbf{G}_{\parallel 1} + \mathbf{G}_{\parallel 2} = P\mathbf{G}_1 + P\mathbf{G}_2 = P(\mathbf{G}_1 + \mathbf{G}_2) = P\mathbf{G}_3 \in \mathcal{G}_\parallel$, where it is clear that $\mathbf{G}_3 \equiv \mathbf{G}_1 + \mathbf{G}_2$ is in $\mathcal{G}$ because $\mathcal{G}$ is a Bravais lattice.

Because $\mathcal{R}_s \subset \mathcal{R}$ it follows from Eq. (A1) that $\mathcal{R}_s \cdot \mathcal{G} \subset 2\pi\mathbb{Z}$. Moreover, because $\mathcal{R}_s \cdot \hat{\mathbf{n}} = 0$, the perpendicular components of all members of $\mathcal{G}$ do not affect the dot product values, and thus we can replace $\mathcal{G}$ with $\mathcal{G}_\parallel$ so that

$$\mathcal{R}_s \cdot \mathcal{G}_\parallel \subset 2\pi\mathbb{Z}.$$

This means that each member of $\mathcal{R}_s$ is among those vectors that always equal 2π times an integer when dotted with any member of $\mathcal{G}_\parallel$. Thus,

$$\mathcal{R}_s \subset \mathcal{G}_\parallel^{-1}, \tag{A2}$$

where $\mathcal{G}_\parallel^{-1}$ denotes the reciprocal lattice of $\mathcal{G}_\parallel$. Note that because $\mathcal{G}_\parallel$ is a two-dimensional Bravais lattice on the surface plane defined by the unit normal vector $\hat{\mathbf{n}}$, $\mathcal{G}_\parallel^{-1}$ is also a two-dimensional Bravais lattice on the same surface plane, and thus $\mathcal{G}_\parallel^{-1} \cdot \hat{\mathbf{n}} = 0$.

We note further that because $\mathcal{G}_\parallel^{-1} \cdot \hat{\mathbf{n}} = 0$, we can replace $\mathcal{G}_\parallel$ with $\mathcal{G}$ in $\mathcal{G}_\parallel^{-1} \cdot \mathcal{G}_\parallel \subset 2\pi\mathbb{Z}$, yielding

$$\mathcal{G}_\parallel^{-1} \cdot \mathcal{G} \subset 2\pi\mathbb{Z},$$

so that $\mathcal{G}_\parallel^{-1} \subset \mathcal{G}^{-1} = \mathcal{R}$. Finally, because $\mathcal{G}_\parallel^{-1} \subset \mathcal{R}$ and $\mathcal{G}_\parallel^{-1} \cdot \hat{\mathbf{n}} = 0$, we find

$$\mathcal{G}_\parallel^{-1} \subset \mathcal{R}_s. \tag{A3}$$

Taken together, equations (A2) and (A3) now imply that $\mathcal{R}_s = \mathcal{G}_\parallel^{-1}$. Finally, because both $\mathcal{R}_s$ and $\mathcal{G}_\parallel^{-1}$ are Bravais lattices, this also means $\mathcal{R}_s^{-1} = \mathcal{G}_\parallel$, so that the set of all $\mathbf{G}_s$ reciprocal to the surface lattice is indeed the same as the set of all $\mathbf{G}_\parallel$, as noted in the main text.

Appendix B: Calculated Mean Transverse Energies at Several Work Functions

Figure 8 shows the MTE of photoelectrons emitted from PbTe(111) as a function of laser photon energy from our measurements and from our calculations at three different work functions: 4.05 eV (used in the present work), 4.2 eV (*ab initio* value from Refs. 24 and 25), and an intermediate value of 4.12 eV. We note that all three work functions yield results with qualitatively similar shapes: a small dip centered at ∼0.05–0.1 eV above the work function, followed by an increase in MTE for ∼0.3–0.4 eV and then a leveling off of the increase. It is apparent that out of the three work functions, 4.05 eV yields calculated MTEs whose overall trends match our experimental results best.

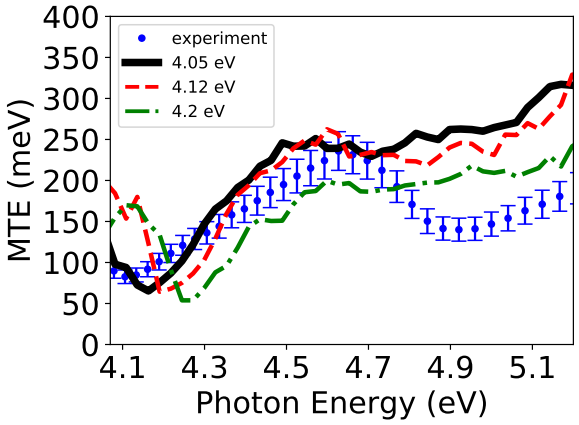

FIG. 8. Mean transverse energy (MTE) of photoelectrons emitted from PbTe(111) as a function of laser photon energy at room temperature: our experimental results (points with error bars), our calculations including both direct and phonon-mediated excitations using a work function of 4.05 eV (solid curve), 4.12 eV (dashed curve), and 4.2 eV (dotted-dashed curve). All three work functions yield curves with similar qualitative shapes, and 4.05 eV yields the best agreement with our experiments.

Finally, we note that for each work function, the calculated MTEs below the work function value correspond to the photoexcitations from conduction states, which have small yet non-zero occupancies at room temperature. The corresponding photocurrents are thus relatively small: for each work function, the photocurrent ∼0.1 eV below the work function is $\sim 10^{-7}$ times the photocurrent at 5 eV.

[1] D. H. Dowell, I. Bazarov, B. Dunham, K. Harkay, C. Hernandez-Garcia, R. Legg, H. Padmore, T. Rao, J. Smedley, and W. Wan, Nucl. Instrum. Methods in Phys. Res. A **622**, 685 (2010).

[2] S. Karkare, W. Wan, J. Feng, T. C. Chiang, and H. A. Padmore, Phys. Rev. B **95**, 075439 (2017).

[3] A. H. Zewail, Annu. Rev. Phys. Chem. **57**, 65 (2006).

[4] P. Emma, R. Akre, J. Arthur, R. Bionta, C. Bostedt, J. Bozek, A. Brachmann, P. Bucksbaum, R. Coffee, F.-J. Decker, Y. Ding, D. Dowell, S. Edstrom, A. Fisher, J. Frisch, S. Gilevich, J. Hastings, G. Hays, P. Hering, Z. Huang, R. Iverson, H. Loos, M. Messerschmidt, A. Miahnahri, S. Moeller, H.-D. Nuhn, G. Pile, D. Ratner, J. Rzepiela, D. Schultz, T. Smith, P. Stefan, H. Tompkins, J. Turner, J. Welch, W. White, J. Wu, G. Yocky, and J. Galayda, Nature Photonics **4**, 641 (2010).

[5] G. Adhikari, P. Riley, and W. A. Schroeder, AIP Advances **9**, 065305 (2019).

[6] R. J. D. Miller, Annu. Rev. Phys. Chem. **65**, 583 (2014).

[7] T. van Oudheusden, E. F. de Jong, S. B. van der Geer,

W. P. E. M. O. 't Root, O. J. Luiten, and B. J. Siwick, J. Appl. Phys. **102**, 093501 (2007).

[8] S. Karkare, J. Feng, X. Chen, W. Wan, F. J. Palomares, T.-C. Chiang, and H. A. Padmore, Phys. Rev. Lett. **118**, 164802 (2017).

[9] S. Karkare, L. Boulet, L. Cultrera, B. Dunham, X. Liu, W. Schaff, and I. Bazarov, Phys. Rev. Lett. **112**, 097601 (2014).

[10] Z. Huang and K.-J. Kim, Phys. Rev. ST Accel. Beams **10**, 034801 (2007).

[11] P. Schmüser, M. Dohlus, and J. Rossbach, *Ultraviolet and Soft X-Ray Free-Electron Lasers* (Springer, Berlin, Heidelberg, 2009).

[12] V. R. Morrison, R. P. Chatelain, K. L. Tiwari, A. Hendaoui, A. Bruhács, M. Chaker, and B. J. Siwick, Science **346**, 445 (2014).

[13] D. Polli, I. Rivalta, A. Nenov, O. Weingart, M. Garavelli, and G. Cerullo, Photochem. Photobiol. Sci. **14**, 213 (2015).

[14] J. Feng, J. Nasiatka, W. Wan, S. Karkare, J. Smedley, and H. A. Padmore, Appl. Phys. Lett. **107**, 134101 (2015).

[15] L. Cultrera, S. Karkare, H. Lee, X. Liu, I. Bazarov, and B. Dunham, Phys. Rev. ST Accel. Beams **18**, 113401 (2015).

[16] P. Musumeci, J. Giner Navarro, J. B. Rosenzweig, L. Cultrera, I. Bazarov, J. Maxson, S. Karkare, and H. Padmore, Nucl. Instrum. Methods Phys. Res. A **907**, 209 (2018).

[17] B. L. Rickman, J. A. Berger, A. W. Nicholls, and W. A. Schroeder, Phys. Rev. Lett. **111**, 237401 (2013).

[18] K. Flöttmann, *Note on the thermal emittance of the electrons emitted by Cesium Telluride photo cathodes*, Tech. Rep. TESLA FEL-Report 1997-01 (DESY, Notkestr. 85, 22603, Hamburg, Germany, 1997).

[19] K. L. Jensen, P. G. O'Shea, D. W. Feldman, and N. A. Moody, Appl. Phys. Lett. **89**, 224103 (2006).

[20] D. H. Dowell and J. F. Schmerge, Phys. Rev. ST Accel. Beams **12**, 074201 (2009).

[21] S. Karkare, D. Dimitrov, W. Schaff, L. Cultrera, A. Bartnik, X. Liu, E. Sawyer, T. Esposito, and I. Bazarov, J. Appl. Phys. **113**, 104904 (2013).

[22] W. A. Schroeder and G. Adhikari, New J. Phys. **21**, 033040 (2019).

[23] N. W. Ashcroft and N. D. Mermin, *Solid State Physics* (Harcourt, 1976) Chap. 9.

[24] W. A. Schroeder, T. Li, and B. Rickman, in *The 4th Photocathode Physics for Photoinjectors, Thomas Jefferson National Accelerator Facility, Newport News, VA, USA* (2016).

[25] T. Li and W. A. Schroeder, "PbTe(111) Sub-Thermionic Photocathode: A Route to High-Quality Electron Pulses," (2017), arXiv:1704.00194.

[26] T. Li, B. L. Rickman, and W. A. Schroeder, J. Appl. Phys. **117**, 134901 (2015).

[27] M. Cardona and D. L. Greenaway, Phys. Rev. **133**, A1685 (1964).

[28] O. Madelung, U. Rössler, and M. Schulz, eds., *Lead telluride (PbTe) crystal structure, lattice parameters, thermal expansion: Datasheet from Landolt-Börnstein - Group III Condensed Matter · Volume 41C: "Non-Tetrahedrally Bonded Elements and Binary Compounds I"* (Springer-Verlag Berlin Heidelberg, 1998) part of SpringerMaterials.

[29] B. Camino, T. C. Q. Noakes, M. Surman, E. A. Seddon, and N. M. Harrison, Comput. Mater. Sci. **122**, 331 (2016).

[30] E. R. Antoniuk, Y. Yue, Y. Zhou, P. Schindler, W. A. Schroeder, B. Dunham, P. Pianetta, T. Vecchione, and E. J. Reed, Phys. Rev. B **101**, 235447 (2020).

[31] P. Borghetti, J. Lobo-Checa, E. Goiri, A. Mugarza, F. Schiller, J. E. Ortega, and E. E. Krasovskii, J. Phys. Condens. Matter **24**, 395006 (2012).

[32] H. Bentmann, H. Maaß, E. E. Krasovskii, T. R. F. Peixoto, C. Seibel, M. Leandersson, T. Balasubramanian, and F. Reinert, Phys. Rev. Lett. **119**, 106401 (2017).

[33] J. Braun, J. Minár, S. Mankovsky, V. N. Strocov, N. B. Brookes, L. Plucinski, C. M. Schneider, C. S. Fadley, and H. Ebert, Phys. Rev. B **88**, 205409 (2013).

[34] J. Braun, J. Minár, and H. Ebert, Phys. Rep. **740**, 1 (2018).

[35] S. Karkare, L. Boulet, L. Cultrera, B. Dunham, X. Liu, W. Schaff, and I. Bazarov, Phys. Rev. Lett. **112**, 097601 (2014).

[36] H. Wu, J. Si, Y. Yan, Q. Liao, and Y. Lu, Appl. Surf. Sci. **356**, 742 (2015).

[37] H.-F. Wu, H.-J. Zhang, Y.-H. Lu, Y.-H. Yan, H.-Y. Li, S.-N. Bao, and P.-M. He, Chinese Phys. B **23**, 127901 (2014).

[38] J. Feng, J. Nasiatka, J. Wong, X. Chen, S. Hidalgo, T. Vecchione, H. Zhu, F. Javier Palomares, and H. A. Padmore, Rev. Sci. Instrum. **84**, 85114 (2013).

[39] J. Feng, J. Nasiatka, W. Wan, T. Vecchione, and H. A. Padmore, Rev. Sci. Instrum. **86**, 15103 (2015).

[40] J. K. Nangoi, T. A. Arias, S. Karkare, H. A. Padmore, and W. A. Schroeder, in *Proceedings of the 9th International Particle Accelerator Conference, Vancouver, BC, Canada, 2018* (JACoW, Geneva, Switzerland, 2018) pp. 1414–1416.

[41] Z. H. Levine and D. C. Allan, Phys. Rev. Lett. **63**, 1719 (1989).

[42] X. Gonze and C. Lee, Phys. Rev. B **55**, 10355 (1997).

[43] G. D. Mahan, Phys. Rev. B **2**, 4334 (1970).

[44] P. J. Feibelman and D. E. Eastman, Phys. Rev. B **10**, 4932 (1974).

[45] J. B. Pendry, Surf. Sci. **57**, 679 (1976).

[46] J. Braun, Reports Prog. Phys. **59**, 1267 (1996).

[47] E. E. Krasovskii and W. Schattke, Phys. Rev. B **56**, 12874 (1997).

[48] E. E. Krasovskii, Phys. Rev. B **70**, 245322 (2004).

[49] E. E. Krasovskii and W. Schattke, Phys. Rev. Lett. **93**, 027601 (2004).

[50] J. Lobo-Checa, J. E. Ortega, A. Mascaraque, E. G. Michel, and E. E. Krasovskii, Phys. Rev. B **84**, 245419 (2011).

[51] A. Damascelli, Z. Hussain, and Z.-X. Shen, Rev. Mod. Phys. **75**, 473 (2003).

[52] R. Sundararaman, P. Narang, A. S. Jermyn, W. A. Goddard III, and H. A. Atwater, Nature Communications **5**, 5788 (2014).

[53] A. M. Brown, R. Sundararaman, P. Narang, W. A. Goddard III, and H. A. Atwater, ACS Nano **10**, 957 (2016).

[54] K. Gottfried and T.-M. Yan, *Quantum Mechanics: Fundamentals*, 2nd ed. (Springer, 2003) Chap. 10.

[55] N. Marzari, A. A. Mostofi, J. R. Yates, I. Souza, and D. Vanderbilt, Rev. Mod. Phys. **84**, 1419 (2012).

[56] N. Marzari and D. Vanderbilt, Phys. Rev. B **56**, 12847 (1997).

[57] J. P. Perdew, K. Burke, and M. Ernzerhof, Phys. Rev. Lett. **77**, 3865 (1996).

[58] D. R. Hamann, Phys. Rev. B **88**, 085117 (2013).

[59] M. Schlipf and F. Gygi, Comput. Phys. Commun. **196**, 36 (2015).

[60] R. Sundararaman, K. Letchworth-Weaver, K. A. Schwarz, D. Gunceler, Y. Ozhabes, and T. A. Arias, SoftwareX **6**,

278 (2017).
[61] A. Goyal, P. Gorai, E. S. Toberer, and V. Stevanović, npj Comput. Mater. **3**, 42 (2017).
[62] H. S. Dow, M. W. Oh, B. S. Kim, S. D. Park, H. W. Lee, and D. M. Wee, in *Proceedings of the XXVI International Conference on Thermoelectrics, Jeju, Korea, 2007* (IEEE, Piscataway, NJ, USA, 2008) p. 90.
[63] W. W. Scanlon, J. Phys. Chem. Solids **8**, 423 (1959).
[64] W. E. Spicer and G. J. Lapeyre, Phys. Rev. **139**, A565 (1965).
[65] K. Weiser, Phys. Rev. B **23**, 2741 (1981).
[66] R. Basu, S. Bhattacharya, R. Bhatt, A. Singh, D. K. Aswal, and S. K. Gupta, J. Elec. Mat. **42**, 2292 (2013).
[67] A. Svane, N. E. Christensen, M. Cardona, A. N. Chantis, M. van Schilfgaarde, and T. Kotani, Phys. Rev. B **81**, 245120 (2010).
[68] W. J. I. DeBenedetti and M. A. Hines, private communication.
[69] P. J. Feibelman, Phys. Rev. Lett. **34**, 1092 (1975).
[70] H. J. Levinson, E. W. Plummer, and P. J. Feibelman, Phys. Rev. Lett. **43**, 952 (1979).
[71] P. J. Feibelman, Prog. Surf. Sci. **12**, 287 (1982).
[72] D. Samuelsen and W. Schattke, Phys. Rev. B **51**, 2537 (1995).
[73] E. E. Krasovskii, V. M. Silkin, V. U. Nazarov, P. M. Echenique, and E. V. Chulkov, Phys. Rev. B **82**, 125102 (2010).
[74] A. Jain, S. P. Ong, G. Hautier, W. Chen, W. D. Richards, S. Dacek, S. Cholia, D. Gunter, D. Skinner, G. Ceder, and K. A. Persson, APL Mater. **1**, 11002 (2013).